Available online at www.sciencedirect.com
SCIENCE DIRECT®
Journal of Sound and Vibration 288 (2005) 957–980
JOURNAL OF SOUND AND VIBRATION
www.elsevier.com/locate/jsvi

Dynamic model of an electromagnetic actuator for vibration control of a cantilever beam with a tip mass

Rong-Fong Fung*, Yung-Tien Liu, Chun-Chao Wang

Department of Mechanical and Automation Engineering, National Kaohsiung First University of Science and Technology, 1 University Road, Yenchau, Kaohsiung 824, Taiwan, ROC

Received 23 June 2004; received in revised form 10 January 2005; accepted 14 January 2005
Available online 10 May 2005

Abstract

The aim of this study is to develop an electromagnetic actuator (EMA) for the vibration control of a cantilever beam with a tip mass. The proposed EMA system consists of an electromagnet and a permanent magnet attached at its top, whereas another permanent magnet is installed at the tip of the cantilever beam. The gravity force is balanced using the repulsive force between the two permanent magnets. The governing equation of the beam vibration coupled with the proposed EMA can be simplified as a bilinear system (BLS). In this study, the PID control, quadratic feedback control and optimal feedback control laws are employed to control the coil currents of electromagnet. The experimental results and numerical solutions reveal that vibrations of the cantilever beam are effectively suppressed by using the proposed EMA with all the three control efforts.

1. Introduction

The control problem of dynamic responses for a cantilever beam with a tip mass is often encountered in many practical engineering applications. To explore the basic nature of the cantilever beam with a tip mass, number of analytical and experimental studies on this issue have been carried out [1,2]. In the mean time, researches on dynamic characteristics of actuators used in

*Corresponding author. Fax: +886 7 6011066.
E-mail address: rffung@ccms.nkfust.edu.tw (R.-F. Fung).

0022-460X/$ - see front matter © 2005 Elsevier Ltd. All rights reserved.
doi:10.1016/j.jsv.2005.01.046

the magnetic levitation system have received attention in the structure control problems. The magnetic levitation techniques not only exploit many advantages of no-mechanical-contact suspension, guidance and propulsion systems, but also utilize the electric current feedback to remove vibration of the levitation body. Schafer and Holzach [1] developed an experimental system for the vibration control of a cantilever beam, in which an optimal regulation for the magnetically levitated body was carried out. In their experiment, the electromagnet was considered to be ideal, and the nonlinear dynamics of the actuator was not taken into consideration. Ju et al. [2] proposed an electromagnetic actuator to the vibration control of a cantilever beam. In their study, both collocated and non-collocated PID controls were used to suppress vibrations of the cantilever beam. By using an ideal permanent magnet and an electromagnet, Nagaya and Arai [3] proposed an actuator in the magnetic levitation system. The analytical expressions for obtaining the levitation force, spring constant, and the control force versus the electric current in the electromagnet were derived using the electromagnetic theory. By using the drag-force-type electromagnetic actuators, Nagaya and Ishikawa [4] proposed a vibration isolation table, which can be moved in both horizontal and vertical directions by magnetic forces. Moreover, Nagaya and Sugiura [5] proposed a permanent magnetic levitation system using a couple of electromagnetic actuators, and found that the feedback for obtaining a linear spring constant has no dependence on the damping force, which is generated by a velocity feedback loop.

The bilinear controller system, perhaps, contains the simplest class of nonlinear system. In general, the control problems for the BLS can be distinguished into three cases [6]: (i) linear feedback control, (ii) quadratic feedback control and (iii) optimal feedback control. Lyapunov stability theorem could be employed to find the stabilizing feedback controller [7] for the continuous BLS such that the closed-loop system is asymptotically stable. Cebuhar and Costanza [8] studied the optimal control problems for the BLS and solved them with a view to approximate analogous problems for the general nonlinear system. The approximation procedure is characterized by a sequence of linear problems converging to the overall optimal solution. Based on Lyapunov stability theorem and the solution of Lyapunov equation, Benallou et al. [9] designed a nonlinear controller, which is similar to the quadratic feedback controller. Chen [10] proposed a novel nonlinear feedback control such that the closed-loop system is not only asymptotically stable but also exponentially stable.

In this study, a cantilever beam is excited in the vertical direction by applying a dc current to the electromagnet. The external nonlinear magnetic force, generated by the EMA, is considered to act on the tip mass. Mathematical expressions of the attraction/repulsive forces are derived using Biot–Savart Law [11]. In addition, the governing equation of motion for the proposed EMA can be simplified as the BLS, which is the main control problem in this paper. Three control strategies, including the PID control, the quadratic feedback control and the optimal feedback control, are applied to suppress the flexible vibrations of the cantilever beam. The dynamic formulations and energetic analysis are discussed. Finally, numerical solutions and experimental results are compared to validate the theoretical analysis.

The paper is organized as follows. Detailed descriptions and theoretical developments on the proposed model are given in Section 2. Mathematical derivations of the controllers are included in Section 3. Numerical simulations and experimental results are given in Section 4. Conclusions are drawn in Section 5.

2. Modeling assumptions and theoretical analysis

2.1. Assumptions

The physical model of the proposed EMA is illustrated in Fig. 1(a), the cantilever beam with tip mass by the Euler-beam theory can be seen in Ref. [12], where ρ is the mass density, A is the cross-sectional area, l is the total length, E is the Young's modulus, and I_n is the moment of inertia of the uniform cantilever beam, which is modeled by the Euler-beam theory. The tip mass is made of the permanent magnet with mass m, and an electromagnetic actuator is employed to control its vibration.

2.2. Kinetic and strain energies

According to the free-body diagram shown in Fig. 1(b), we have the shear force $v = -mg$ and the moment–shear relationship $dM/dx = -v$. By using the boundary conditions $v(0,t) = v_x(0,t) = 0$ and $v_{xx}(l,t) = 0$, it is easy to obtain the deflection

$$v(x,t) = v(l,t)\left[\frac{3}{2}\left(\frac{x}{l}\right)^2 - \frac{1}{2}\left(\frac{x}{l}\right)^3\right] \tag{1}$$

where $v(l,t) = -mgl^3/(3EI_n)$ is the tip deflection of the cantilever beam subjected to a tip loading mg, and EI_n is the bending rigidity of the beam.

Energy methods [12] can be used to find the approximate equation of motion of the system in Fig. 1(a), and its equivalent mass-spring system is shown in Fig. 1(c). The elasticity of the cantilever beam is lumped as an equivalent spring with an elastic constant K_e, while the inertial properties of the cantilever beam and its tip mass are lumped as an equivalent mass M_e.

By using Eq. (1), the kinetic energy of the cantilever beam and its tip mass can be written as

$$\text{K.E.} = \frac{1}{2}\int_0^l \rho A v_t^2(x,t)\,dx + \frac{1}{2}mv_t^2(l,t) = \frac{1}{2}M_e v_t^2(l,t), \tag{2a}$$

where $M_e = (33/140)\rho Al + m$, and $v_t(l,t)$ is the velocity of the tip mass.

The strain energy of the cantilever beam can be written as

$$\text{S.E.} = \int_0^l \frac{1}{2}EI_n v_{xx}^2(x,t)\,dx = \frac{1}{2}K_e v^2(l,t), \tag{2b}$$

where $K_e = (3EI_n)/l^3$.

For an underdamped system, one cycle apart from free vibrations decay can be measured exponentially in Fig. 1(d), which along with the logarithmic decrement δ are given in Ref. [13] as

$$\delta = \ln\left(\frac{z_1}{z_2}\right) = \frac{2\pi\zeta}{\sqrt{1-\zeta^2}} = \frac{2\pi}{\omega_d}\frac{C_e}{2M_e}, \tag{2c}$$

where

$$\tau_d = \frac{2\pi}{\omega_d} = \frac{2\pi}{\omega_n\sqrt{1-\zeta^2}} \text{ is the period of damped vibration,}$$

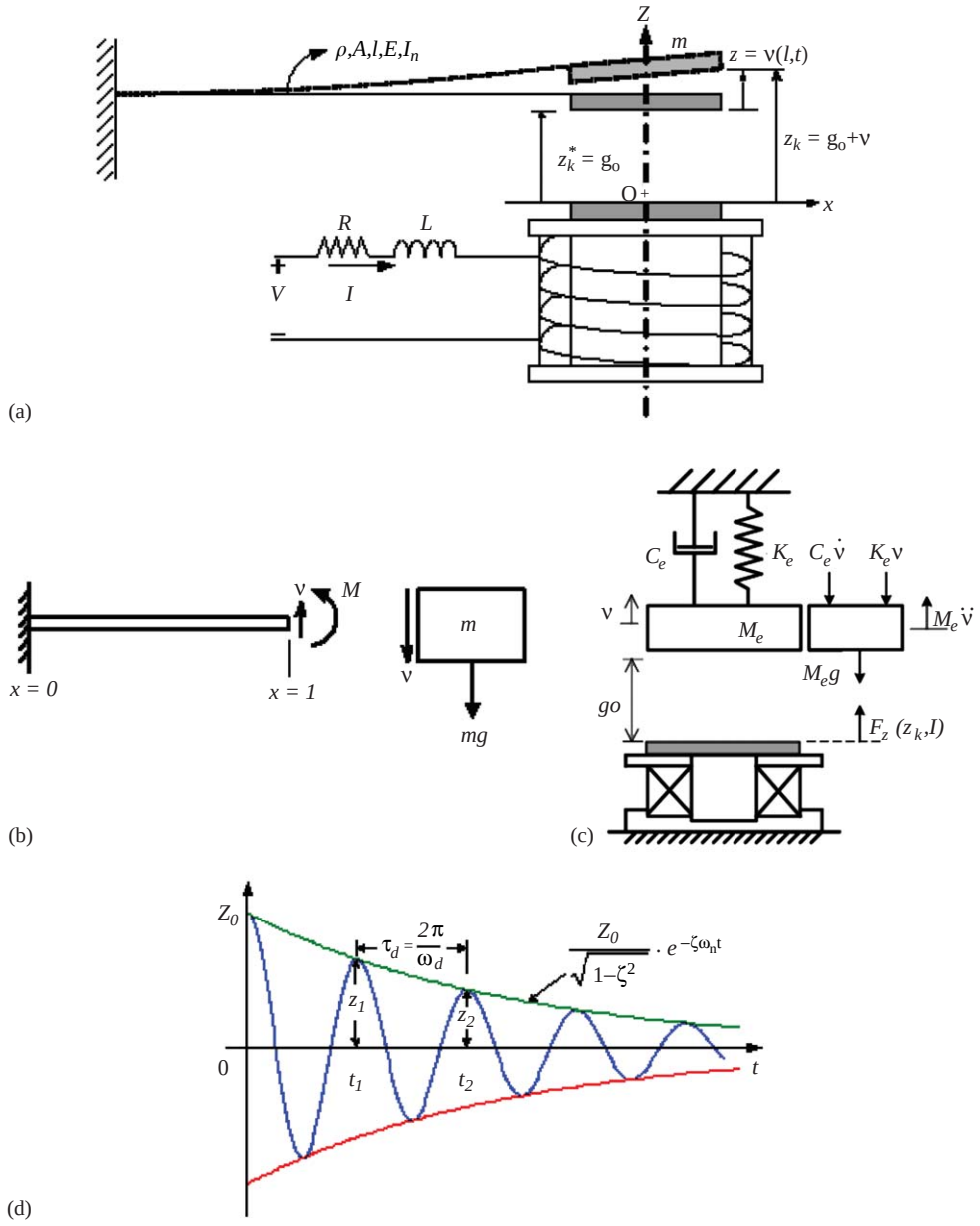

Fig. 1. Schematic diagram of the system. (a) The cantilever beam with a tip mass excited by an electromagnetic actuator. (b) The free-body diagram of the system at $x = l$. (c) The equivalent system.

$$\zeta = \frac{C_e}{2\sqrt{K_e M_e}} \text{ is defined as damping ratio,}$$

$$\omega_d = \omega_n\sqrt{1-\zeta^2} \text{ is the frequency of damped vibration,}$$

$\omega_n = \sqrt{\dfrac{K_e}{M_e}}$ is the undamped natural frequency.

From Eqs. (2a) and (2b), we obtain two equivalent parameters: elastic constant K_e and equivalent mass M_e. On substituting them into Eq. (2c), we can obtain the damping constant C_e. By using the equivalent model with the elastic constant K_e, the damping constant C_e, and the mass M_e, the equation of motion is easily derived and the system becomes 1 dof. The total mechanical energy is the combination of the kinetic energy (2a) and strain energy (2b).

2.3. Modeling of the electromagnetic actuator

Fig. 2 illustrates the coordinates of the EMA including an electromagnet and a permanent magnet attached at the cantilever tip. The coordinates and symbols are defined as follows: a_1 is the width of a rectangular permanent magnet, a_2 is the outer width of the coil, b_1 is the length of a rectangular permanent magnet, b_2 is the outer thickness of the coil; z_1 is the coordinate describing the upper surface of the permanent magnet at the cantilever tip, z_2 and z_3 are the coordinates describing the upper and lower ends of the core of the electromagnet, respectively; z_{e1} and z_{e2} are the coordinates describing the upper and lower ends of the coil of the electromagnet, respectively; and z_k is the gap between the two magnets.

Figs. 3(a)–(e) and 4 illustrate the current and magnetic flux of a rectangular coil. Fig. 3(a) illustrates the geometry of one turn rectangular current. Fig. 3(b) illustrates magnetic flux at the point P due to the current AB. Figs. 3(c) and (d) illustrate magnetic flux at the point P due to the current AB mapping on the zx and zy planes, respectively. Fig. 3(e) illustrates magnetic fluxes at the point P due to the coil current of N turns. It is seen that the magnetic flux densities due to the coil current [4], at an arbitrary point (x, y, z) due to an input current I flowing through a rectangular coil can be expressed as

$$B_{esx}(x, y, z) = \mu_0 j F_{esx}(x, y, z), \tag{3a}$$

$$B_{esy}(x, y, z) = \mu_0 j F_{esy}(x, y, z), \tag{3b}$$

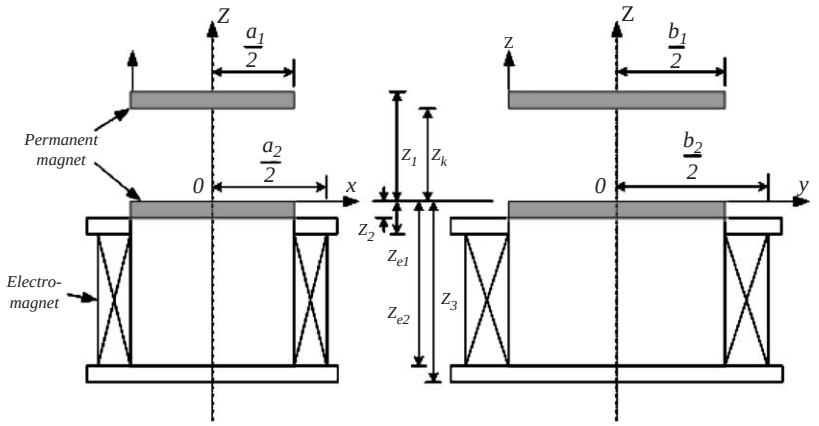

Fig. 2. Coordinates of the proposed electromagnetic actuator.

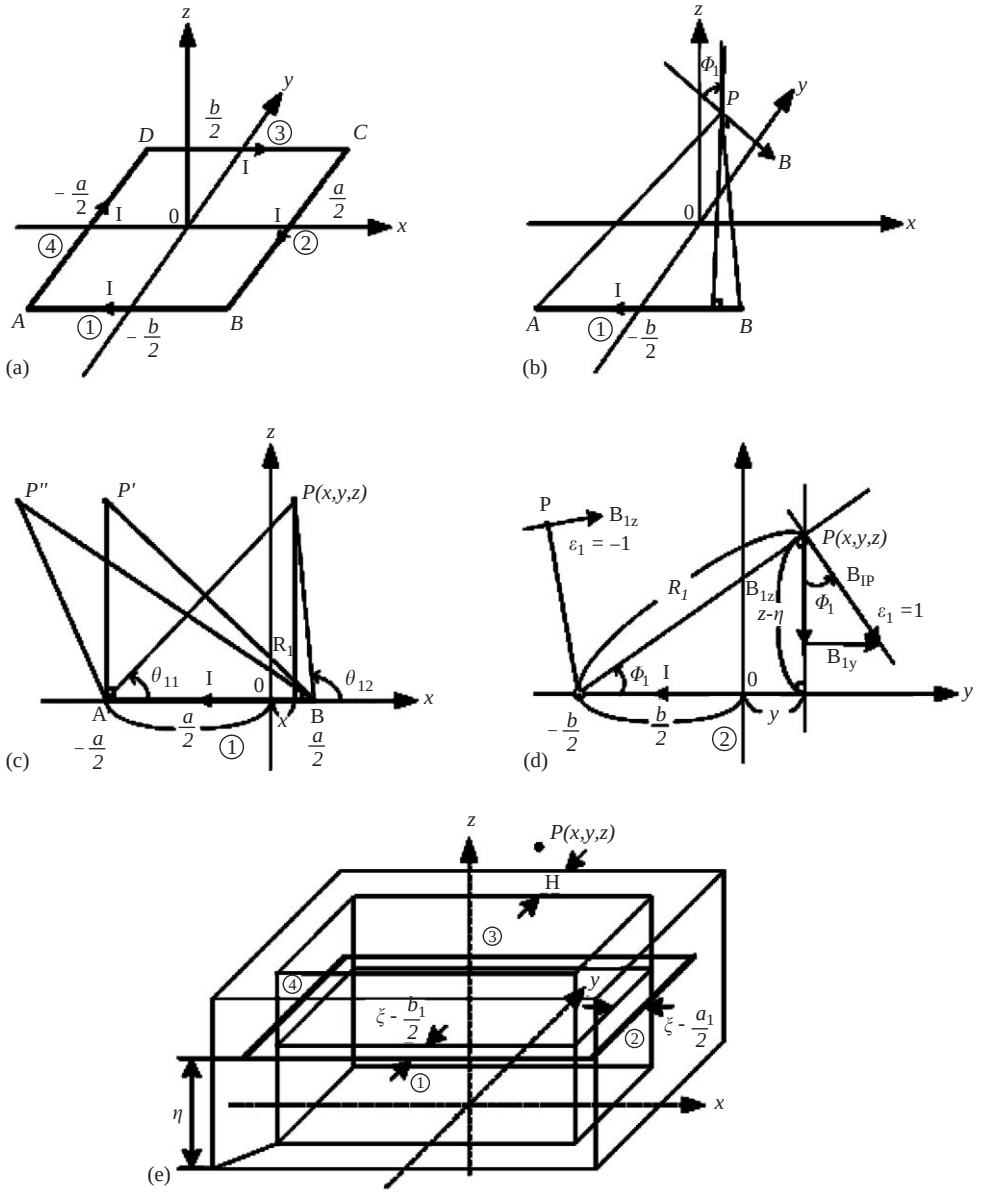

Fig. 3. Coordinates of the rectangular currents. (a) Geometry of one turn rectangular current. (b) Magnetic flux at point P due to the current AB. (c) and (d) Magnetic fluxes at the point P due to the current AB in the *xz* and *yz* planes, respectively. (e) Magnetic fluxes at the point P due to the coil currents of N turns.

$$B_{esz}(x, y, z) = \mu_0 j F_{esz}(x, y, z), \tag{3c}$$

where

$$j = j_x = j_y, \tag{3d}$$

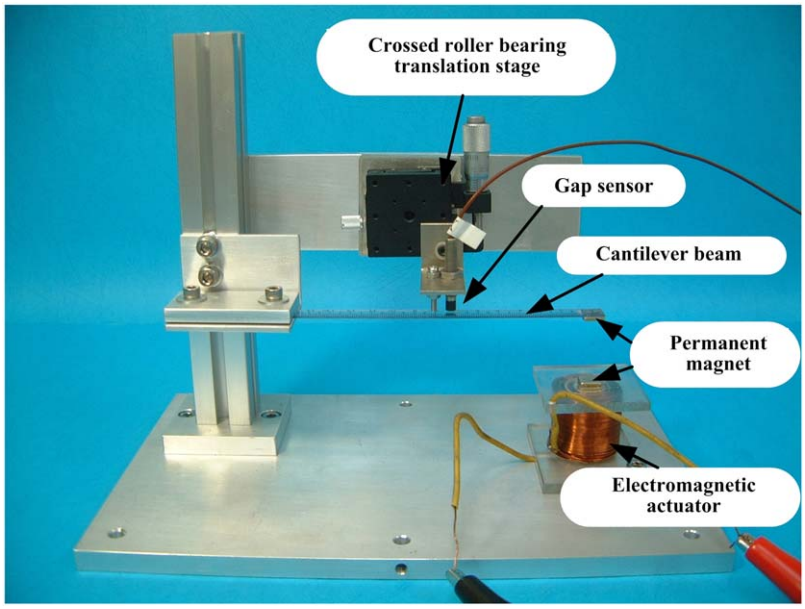

Fig. 4. Photograph of the experimental cantilever beam with the EMA.

$$j_x = \frac{N}{(\frac{a_2}{2} - \frac{a_1}{2})H} I \quad \text{for the coil in the } x \text{ direction,}$$

$$j_y = \frac{N}{(\frac{b_2}{2} - \frac{b_1}{2})H} I \quad \text{for the coil in the } y \text{ direction,}$$

in which μ_0 is the magnetic permeability in air, j is the electric current per unit cross-sectional area in the coil, N is the number of turns of the coil, and H represents the height of the coil ($z_{e1} - z_{e2}$). The detailed parameters of Eqs. (3)–(9) can be seen in Appendix A. In addition, it is assumed that the width and thickness of rectangular coil are equal in the x and y directions (i.e. $a_2/2 - a_1/2 = b_2/2 - b_1/2$), and one will have $j = j_x = j_y$. The detailed derivatives can be seen in Ref. [4].

The magnetic flux densities due to the core under the input current I are

$$B_{ecx}(x, y, z) = J_{ce}(I) F_{ecx}(x, y, z), \tag{4a}$$

$$B_{ecy}(x, y, z) = J_{ce}(I) F_{ecy}(x, y, z), \tag{4b}$$

$$B_{ecz}(x, y, z) = J_{ce}(I) F_{ecz}(x, y, z), \tag{4c}$$

where

$$J_{ce}(I) = \mu \frac{NI}{z_2} = \mu_0 \mu_r \frac{NI}{z_2}. \tag{4d}$$

In Eq. (4d), μ_r denotes the relative permeability of the electromagnet core. Since the electromagnet and permanent magnet are connected together at boundary $z = z_2$, the core of the electromagnet can be magnetized by the permanent magnet. The magnetization strength J_{cp} in the core due to the permanent magnet can be found by using

$$J_{\mathrm{cp}} = \frac{G_{\mathrm{cp}}}{G_p}(1 - v)J_0, \tag{5}$$

where J_0 is the strength of magnetization of the permanent magnet, and v is the leak coefficient.

The magnetic flux densities B_{px}, B_{py}, and B_{pz} at a point P induced by both the permanent magnet and the magnetized core are obtained by summing the flux densities due to J_0 and J_{cp} as

$$B_{px}(x, y, z) = J_0 F_{px}(x, y, z) + J_{\mathrm{cp}} F_{ecx}(x, y, z), \tag{6a}$$

$$B_{py}(x, y, z) = J_0 F_{py}(x, y, z) + J_{\mathrm{cp}} F_{ecy}(x, y, z), \tag{6b}$$

$$B_{pz}(x, y, z) = J_0 F_{pz}(x, y, z) + J_{\mathrm{cp}} F_{ecz}(x, y, z). \tag{6c}$$

With the opposite polarity, the magnetic flux densities B_{mx}, B_{my}, and B_{mz} at the point P induced by the permanent magnet of the cantilever tip are

$$B_{mx}(x, y, z) = J_0 F_{mx}(x, y, z), \tag{7a}$$

$$B_{my}(x, y, z) = J_0 F_{my}(x, y, z), \tag{7b}$$

$$B_{mz}(x, y, z) = J_0 F_{mz}(x, y, z). \tag{7c}$$

Hence, the magnetic flux densities B_{fx}, B_{fy}, and B_{fz} due to the entire coil, permanent magnet, and the core of electromagnet are

$$B_{fx}(x, y, z, I) = B_{esx}(x, y, z, I) + B_{ecx}(x, y, z, I) + B_{px}(x, y, z, I), \tag{8a}$$

$$B_{fy}(x, y, z, I) = B_{esy}(x, y, z, I) + B_{ecy}(x, y, z, I) + B_{py}(x, y, z, I), \tag{8b}$$

$$B_{fz}(x, y, z, I) = B_{esz}(x, y, z, I) + B_{ecz}(x, y, z, I) + B_{pz}(x, y, z, I). \tag{8c}$$

Since opposite polarities face each other, the total magnetic flux densities B_x, B_y, and B_z are

$$B_x(x, y, z, I) = B_{fx}(x, y, z, I) - B_{mx}(x, y, z), \tag{9a}$$

$$B_y(x, y, z, I) = B_{fy}(x, y, z, I) - B_{my}(x, y, z), \tag{9b}$$

$$B_z(x, y, z, I) = B_{fz}(x, y, z, I) - B_{mz}(x, y, z). \tag{9c}$$

2.4. Magnetic force

The total force vector $\mathbf{F}$ in the magnetic field is obtained by using Maxwell's stress tensors, which can be seen in Refs. [3–5]:

$$\mathbf{F} = \iint_a \mathbf{T} \cdot \hat{n}\, \mathrm{d}a, \tag{10a}$$

where $\mathbf{T}$ is the stress tensor in the magnetic field and $\hat{n} = \hat{n}_x n_x + \hat{n}_y n_y + \hat{n}_z n_z$ is the normal vector of a small area da. $\mathbf{T}$ is shown by using the orthogonal coordinates (x, y, z) as follows:

$$\mathbf{T} = \begin{bmatrix} T_{xx} & T_{xy} & T_{xz} \\ T_{yx} & T_{yy} & T_{yz} \\ T_{zx} & T_{zy} & T_{zz} \end{bmatrix} = \frac{1}{\mu_0} \begin{bmatrix} \dfrac{B_x^2 - B_y^2 - B_z^2}{2} & B_x B_y & B_x B_z \\ B_y B_x & \dfrac{-B_x^2 + B_y^2 - B_z^2}{2} & B_y B_z \\ B_z B_x & B_z B_y & \dfrac{-B_x^2 - B_y^2 + B_z^2}{2} \end{bmatrix}. \tag{10b}$$

The interactive force $F_z(z_k, I)$ of the EMA is then expressed as

$$F_z(z_k, I) = \iint_a (T_{zx}\hat{n}_x + T_{zy}\hat{n}_y + T_{zz}\hat{n}_z)\,\mathrm{d}a. \tag{11a}$$

Since the magnetic field is symmetrical about the z-axis, the components of the normal vector become $n_x = n_y = 0$. Substituting these into Eq. (11a), yields

$$F_z(z_k, I) = \frac{1}{2\mu_0} \int_{-a_1/2}^{a_1/2} \int_{-b_1/2}^{b_1/2} [B_z^2(x, y, z_k, I) - B_x^2(x, y, z_k, I) - B_y^2(x, y, z_k, I)]\,\mathrm{d}x\,\mathrm{d}y. \tag{11b}$$

Substituting Eq. (9) into Eq. (11b), the actuating force has the form

$$F_z(z_k, I) = \alpha_2(z_k) I^2 + \alpha_1(z_k) I + F_s(z_k), \tag{11c}$$

where $\alpha_2(z_k)$, $\alpha_1(z_k)$ and $F_s(z_k)$ represent the coefficients, which are functions of the air gap z_k. The details can be seen in Appendix B.

2.5. Control force

In Fig. 1(a), $z_k^* = g_0$ is the equilibrium position of air gap between the two permanent magnets, one is attached to the electromagnet and the other is attached at the tip of the cantilever beam. In this static equilibrium, we have the input current $I = 0$. According to Eq. (11c), the corresponding actuating force is given by

$$F_z(z_k^*, 0) = F_s(z_k^*). \tag{12a}$$

Define the control force under the non-zero input current I as

$$\begin{aligned} F_c(z_k, I) &= F_z(z_k, I) - F_s(z_k^*) \\ &= \alpha_2(z_k) I^2 + \alpha_1(z_k) I + [F_s(z_k) - F_s(z_k^*)]. \end{aligned} \tag{12b}$$

The forces generated by the electromagnetic actuator are dependent on the input currents and air gaps between the two permanent magnets. From the calibration results of the magnetic force, it is found that the term $\alpha_2(z_k) I^2$ is much smaller than the other terms in Eq. (12b), especially when the current is so small that it can be neglected. The electromagnetic forces, described by using a multiple linear regression model [14] with the ANOVA (Analysis of Variance Table) analysis

Table 1
The ANOVA analysis table of the multiple regression method

The regression equation is: $F_c(z_k, I) = 6.40 \times 10^{-3} z_k + 1.60 \times 10^{-2} I + 5.46 \times 10^{-1} z_k I$

Multiple R	99.8%	Analysis of variance					
R square	99.7%		DF	Sum of squares	Mean square	F	PROB$>F$
Adjusted R square	99.6%	Regression	$k = 3$	1.51E+0	5.05E−1		
Standard error	1.54E−3	Residual	$n - k - 1 = 1997$	4.74E−3			
Observation number	2001	Total	$n - 1 = 2000$	1.52E+0			

Variables in the equation

Predictor	Coefficient	Stdev	t-ratio	P-values
$\beta_1(Z_k)$	6.40E−3	1.65E−3	3.87E+0	1.12E−4
$\beta_2(I)$	1.60E−2	8.74E−4	1.83E+1	0.00E+0
$\beta_3(Z_k I)$	5.46E−1	2.73E−2	1.98E+1	0.00E+0

listed in Table 1 are reduced as

$$\begin{aligned} F_c(z_k, I) &\approx \alpha_1(z_k) I + [F_s(z_k) - F_s(z_k^*)] \\ &\approx \beta_1 z_k + \beta_2 I + \beta_3 z_k I, \end{aligned} \tag{12c}$$

where $z_k = g_0 + v(l, t)$.

$$\begin{aligned} F_c(z_k, I) &\approx \beta_1(g_0 + v) + \beta_2 I + \beta_3(g_0 + v) I \\ &\approx \beta_1 g_0 + \beta_1 v + (\beta_2 + \beta_3 g_0) I + \beta_3 v I. \end{aligned} \tag{12d}$$

In the ANOVA analysis, the squared correlation between the real values and fitted values is called the square of multiple correlation coefficients, usually labeled "R-square". The idea is that R-square value gives some sense about the agreement between the observed values, and the predicted values resulting from the regression equation. The value of R-square is between 0 and 1, and as we increase the number of predictors, R-square gets larger. This form of multiple linear regression models can be found in Appendix C.

2.6. Equation of motion

The equation of motion of the equivalent model in Fig. 1(c), which is excited by the control force, can be easily obtained by using Eqs. (2a)–(2c) as

$$F_z(z_k, I) - M_e g - C_e \dot{v}(l, t) - K_e v(l, t) = M_e \ddot{v}(l, t), \tag{13a}$$

$$M_e \ddot{v}(l, t) + C_e \dot{v}(l, t) + K_e v(l, t) = F_c(z_k, I), \tag{13b}$$

where $F_z(z_k, I) = F_c(z_k, I) + F_s(z_k^*)$ and $F_s(z_k^*) = M_e g$.

In the following, we consider the case of small vibrations with the coefficient $z_k = g_0 + v(l,t)$. Hence, Eq. (13) can be simplified as

$$M_e\ddot{v} + C_e\dot{v} + (K_e - \beta_1)v = \beta_1 g_0 + \beta_4 I + \beta_3 I v, \tag{14}$$

where $\beta_4 = \beta_2 + \beta_3 g_0$.

If the control current I of the coil system is given as $I = I_0 + I_C$, where I_0 and I_C are the steady current and the control current, respectively. Then the equation of motion for the cantilever beam with a tip mass can be expressed as

$$M_e\ddot{v} + C_e\dot{v} + (K_e - \beta_5)v = \beta_6 + \beta_4 I_C + \beta_3 I_C v, \tag{15}$$

where

$$\beta_5 = \beta_1 + \beta_3 I_0 \quad \text{and} \quad \beta_6 = \beta_1 g_0 + \beta_4 I_0.$$

Considering the case of the steady-state situation, i.e., $\ddot{v} = \dot{v} = 0$ and $v =$ constant, then Eq. (14) without the control current can be rewritten as

$$(K_e - \beta_5)v_s = \beta_6. \tag{16}$$

Thus, we have the steady-state displacement $v_s = \beta_6/(K_e - \beta_5)$.

In order to simply the dynamic analysis, let $w = v - v_s$, and one will have $\ddot{w} = \ddot{v}$ and $\dot{w} = \dot{v}$. Therefore, Eq. (15) can be rewritten as

$$M_e\ddot{w} + C_e\dot{w} + (K_e - \beta_5)w = \beta_7 I_C + \beta_3 I_C w, \tag{17}$$

where $\beta_7 = \beta_4 + \beta_3 v_s$. It should be noted that the variable w is coupled with the control input I_C in Eq. (17), which is a standard form of a bilinear equation [6].

The dynamic equation (17) can be further expressed in the state-space form

$$\dot{\mathbf{X}} = \mathbf{A}\mathbf{X} + \mathbf{N}\mathbf{X}U + \mathbf{B}U = \mathbf{A}\mathbf{X} + (\mathbf{N}\mathbf{X} + \mathbf{B})U, \quad \mathbf{X}(0) = \mathbf{X}_0, \tag{18}$$

where $\mathbf{X} = \{w \;\; \dot{w}\}^{\mathrm{T}} \in R^2$, $U = V = I_C R$ can be regarded as an equivalent circuit, and the matrices $\mathbf{A}, \mathbf{N}$, and the vector $\mathbf{B}$ are

$$\mathbf{A} = \begin{bmatrix} 0 & 1 \\ \dfrac{\beta_5 - K_e}{M_e} & -\dfrac{C_e}{M_e} \end{bmatrix} \in R^{2\times 2}, \quad \mathbf{N} = \begin{bmatrix} 0 & 0 \\ \dfrac{\beta_3}{RM_e} & 0 \end{bmatrix} \in R^{2\times 2}, \tag{19a–b}$$

$$\mathbf{B} = \begin{bmatrix} 0 \\ \dfrac{\beta_7}{RM_e} \end{bmatrix} \in R^{2\times 1}. \tag{19c}$$

The controller design will be formulated from Eq. (18) such that $\boldsymbol{X} \to 0$ and $\boldsymbol{U} \to 0$ as $t \to \infty$.

3. Controller design

In this section, the PID control, the quadratic feedback control and the optimal feedback control will be designed for the bilinear equation (18). Both the numerical simulations and experimental verifications of a cantilever beam with the proposed EMA will be performed with all the three controllers.

3.1. The PID control

The structure of a typical PID (Proportional-plus-Integral-plus-Derivative) controller is very simple in the control loops, which can be easily understood and implemented in practice. Such a simple PID control scheme is given by

$$I_C(z) = \left[K_p + K_i \frac{T}{2}\left(\frac{z+1}{z-1}\right) + K_d\left(\frac{z-1}{Tz}\right)\right] w(z), \tag{20}$$

where $I_C(z)$ represents the control current as a transfer function of z, T is the sampling interval of the control system is 1 ms, and $w(z)$ is the z-transform of the displacement error of the cantilever beam. The derivative control is realized by a low-pass filter by a cutoff frequency of $2/T$. The parameters used for simulation are listed in Table 2.

3.2. Quadratic feedback control

A quadratic Lyapunov function candidate $V(\mathbf{X}) = 1/2\mathbf{X}^{\mathrm{T}}\mathbf{S}\mathbf{X}$ is chosen for the feedback control design. Based on the chosen $V(\mathbf{X})$, we can design the quadratic feedback control [7] as

$$I_C = -\alpha(\mathbf{N}\mathbf{X} + \mathbf{B})^{\mathrm{T}}\mathbf{S}\mathbf{X} \tag{21}$$

which will stabilize Eq. (18). Here $\alpha > 0$, and $\mathbf{S}$ is a real positive definite 2×2 matrix that satisfies Lyapunov equation:

$$\mathbf{A}^{\mathrm{T}}\mathbf{S} + \mathbf{S}\mathbf{A} + \mathbf{Q} = \mathbf{0}, \tag{22}$$

where $\mathbf{Q}$ is a real positive semi-definite 2×2 matrix.

The proof may be obtained from the rate of change of the quadratic Lyapunov function candidate for (25). The result is given by

$$\dot{V}(\mathbf{X}) = -\tfrac{1}{2}\mathbf{X}^{\mathrm{T}}\mathbf{Q}\mathbf{X} - \alpha[\mathbf{X}^{\mathrm{T}}\mathbf{S}(\mathbf{N}\mathbf{X} + \mathbf{B})]^2, \tag{23}$$

where $V(\mathbf{X}) > 0$ and $\dot{V}(\mathbf{X}) < 0$ for all $\boldsymbol{X} \neq \mathbf{0}$. Otherwise, it can also be shown in Ref. [9] that the set $\Sigma = \{\boldsymbol{X} \in R^2 : \dot{V}(\boldsymbol{X}) = 0\}$ has a unique solution and contains only trivial trajectories of Eq. (18).

Table 2
The parameters of the system

Strength of magnetization of the permanent magnet	$J_0 = 0.85$	(T)
Width of rectangular permanent magnet	$a_1 = 10 \times 10^{-3}$	(m)
Outer width of the coil	$a_2 = 17.5 \times 10^{-3}$	(m)
Length of a rectangular permanent magnet	$b_1 = 10 \times 10^{-3}$	(m)
Outer length of the coil	$b_2 = 17.5 \times 10^{-3}$	(m)
Height of the coil ($z_{e1} - z_{e2}$)	$H = 30 \times 10^{-3}$	(m)
Height of the core ($z_2 - z_3$)	$H_c = 31.5 \times 10^{-3}$	(m)
Number of turns of the coil	N = 572	
Mass of the permanent magnet	$m = 4.0 \times 10^{-3}$	(kg)
Resistance of the coil	$R = 2.1$	(Ω)
Inductance of the coil	$L = 9.7 \times 10^{-3}$	(h)

Hence, the control current I_C in Eq. (21) globally asymptotically stabilizes the bilinear system (18).

3.3. Optimal feedback control

To solve the optimal control problem of the bilinear system (18), the quadratic performance index is defined as follows:

$$J(\mathbf{X}, I_C) = \frac{1}{2}\int_0^\infty [\mathbf{X}^{\mathrm{T}}\mathbf{Q}\mathbf{X} + rI_C^2]\,\mathrm{d}t, \tag{24}$$

where $\mathbf{Q}$ is a real positive semi-definite 2×2 matrix, and r is a real positive value. By using Hamilton–Jacobi–Bellman (HJB) equation [15], Hamiltonian of the system can be formed as

$$H(\mathbf{X}, \mathbf{V}_x^*, I_C) = \tfrac{1}{2}[\mathbf{X}^{\mathrm{T}}\mathbf{Q}\mathbf{X} + rI_C^2] + (\mathbf{V}_x^*)^{\mathrm{T}}[\mathbf{A}\mathbf{X} + (\mathbf{N}\mathbf{X} + \mathbf{B})\mathbf{I}_C], \tag{25}$$

where $V^*(\mathbf{X})$ is a quadratic function of the state. It seems reasonable to guess a solution in the form: $V^*(\mathbf{X}) = (1/2)\mathbf{X}^{\mathrm{T}}\mathbf{S}(\mathbf{X})\mathbf{X}$, and the solution of the HJB equation for the infinite-time case is in the form: $V_{\mathbf{x}}^* = \mathbf{S}(\mathbf{X})\mathbf{X}$, where the matrix-valued function $\mathbf{S}(\mathbf{X})$ is real positive definite. Applying the necessary condition for a minimum: $\partial H/\partial I_C = 0$ and $\partial^2 H/\partial I_C^2 \geqslant 0$ [17], we obtain the expression for the optimal control current I_C^* as follows:

$$I_C^* = -r^{-1}[\mathbf{N}\mathbf{X} + \mathbf{B}]^{\mathrm{T}}\mathbf{S}(\mathbf{X})\mathbf{X}. \tag{26}$$

It can be seen that the designed optimal feedback control law in Eq. (26) is similar to the quadratic feedback control law in Eq. (21). The matrix-valued function $\mathbf{S}(\mathbf{X})$ can be obtained from the time-varying algebraic Riccati equation:

$$\mathbf{A}^{\mathrm{T}}\mathbf{S}(\mathbf{X}) + \mathbf{S}(\mathbf{X})\mathbf{A} - \mathbf{S}(\mathbf{X})[\mathbf{N}\mathbf{X} + \mathbf{B}]r^{-1}[\mathbf{N}\mathbf{X} + \mathbf{B}]^{\mathrm{T}}\mathbf{S}(\mathbf{X}) + \mathbf{Q} = \mathbf{0} \tag{27}$$

Substituting I_C^* of Eq. (26) into Hamiltonian (25) via Eq. (27), it yields $H(\mathbf{X}, V_{\mathbf{x}}^*, I_C^*) = 0$, and shows that the performance index is minimized by I_C^*. The proof of the global asymptotic stability [15] is the same as Eq. (23).

Unfortunately, this nonlinear system of algebraic matrix equation (18) is hard to solve. In other words, it has no analytical solution. However, it has been shown in Ref. [16] that the approximate solutions can be obtained using the iteration method from the convergent sequence of the following linear system:

(a) if $\mathbf{X}^{(0)}(0) = \mathbf{X}_0$, $j = 0$,

$$\dot{\mathbf{X}}^{(0)} = \mathbf{A}\mathbf{X}^{(0)}; \tag{28}$$

(b) if $\mathbf{X}^{(j)}(0) = \mathbf{X}_0$, $j = 1, 2, \ldots$,

$$\dot{\mathbf{X}}^{(j)} = \mathbf{A}\mathbf{X}^{(j)} + (\mathbf{N}\mathbf{X}^{(j-1)} + \mathbf{B})I_C^{(j)}. \tag{29}$$

Therefore, the related sequence of the time-varying algebraic Riccati equation and the suitable optimal control current are listed as follows:

$$\mathbf{A}^{\mathrm{T}}\mathbf{S}^{(j)} + \mathbf{S}^{(j)}\mathbf{A} - \mathbf{S}^{(j)}(\mathbf{N}\mathbf{X}^{(j-1)} + \mathbf{B})r^{-1}(\mathbf{N}\mathbf{X}^{(j-1)} + \mathbf{B})^{\mathrm{T}}\mathbf{S}^{(j)} + \mathbf{Q} = \mathbf{0}, \tag{30}$$

$$I_C^{*(j)} = -r^{-1}[\mathbf{N}\mathbf{X}^{(j-1)} + \mathbf{B}]^{\mathrm{T}}\mathbf{S}^{(j)}\mathbf{X}^{(j)}. \tag{31}$$

The trajectories $\mathbf{X}^{*(j)}$ are the solutions of Eq. (29) associated with $I_C^{*(j)}$ in place of I_C. It has been proved [16] that if $\mathbf{X}^*$ and I_C^* represent the solutions of the optimization problem (18) and (27), then the sequence $\{\mathbf{X}^{*(j)}\}$ converges uniformly to the optimal trajectory $\mathbf{X}^*$ and the sequence $\{I_C^{*(j)}\}$ converges uniformly to the optimal control I_C^*.

4. Numerical and experimental results

4.1. Physical model

4.1.1. System parameters

In the numerical simulations, Runge–Kutta method is employed to solve Eq. (18). The system parameters are chosen as follows:

(i) *Cantilever beam*: $l = 0.146\,\mathrm{m}$, $b = 0.01\,\mathrm{m}$, $h = 0.001\,\mathrm{m}$, $\rho = 411\,\mathrm{kg/m^3}$, $E = 20\,\mathrm{GPa}$, $A = 1.0 \times 10^{-5}\,\mathrm{m^2}$, and $I_n = 8.33 \times 10^{-13}\,\mathrm{m^4}$;
(ii) *Tip mass*: $m = 4 \times 10^{-3}\,\mathrm{kg}$;
(iii) *The other parameters*: $g_0 = 3.2 \times 10^{-2}\,\mathrm{m}$, and $I_0 = 0\,\mathrm{A}$.

4.1.2. Initial conditions

In the numerical simulations, the initial conditions of the cantilever beam at the tip are $v(l,0) = 3.46 \times 10^{-3}\,\mathrm{m}$ and $v_t(l,0) = 0\,\mathrm{m/s}$.

4.2. Control parametric matrices

The design technique of the quadratic and optimal feedback controls for the bilinear system can be summarized in the following steps:

Step 1: Choose the weighting matrices:

$$\mathbf{Q} = \begin{bmatrix} 5 & 0 \\ 0 & 5 \end{bmatrix} \in R^{2\times 2}.$$

Step 2: Choose the weighting factors:

(i) Quadratic feedback control: $\alpha = 1 \times 10^{-3}$.
(ii) Optimal feedback control: $r = 0.05$.

Step 3: Solve Lyapunov equation (22) for **S** in the quadratic feedback control method or solve the time-varying algebraic Riccati equation (27) for **S**(**X**) in the optimal feedback control method.

Step 4: Obtain the control currents from Eqs. (21) and (26).

4.3. Experimental setup

Fig. 5 shows the photograph of the experimental cantilever beam with the EMA. The input voltage waveform of the electromagnetic actuator is generated by the SIMULINK software and Real-Time Windows Target Tool, which is a Windows-supported graphical programming language. The DA/AD converter with a resolution of 12 bits is used to transform the output waveform to the power amplifier, and then to the EMA. A capacitor-type sensor (ADE: Model-5503) with the frequency bandwidth of 20 kHz, the measuring range of $\pm 500\,\mu m$ and the

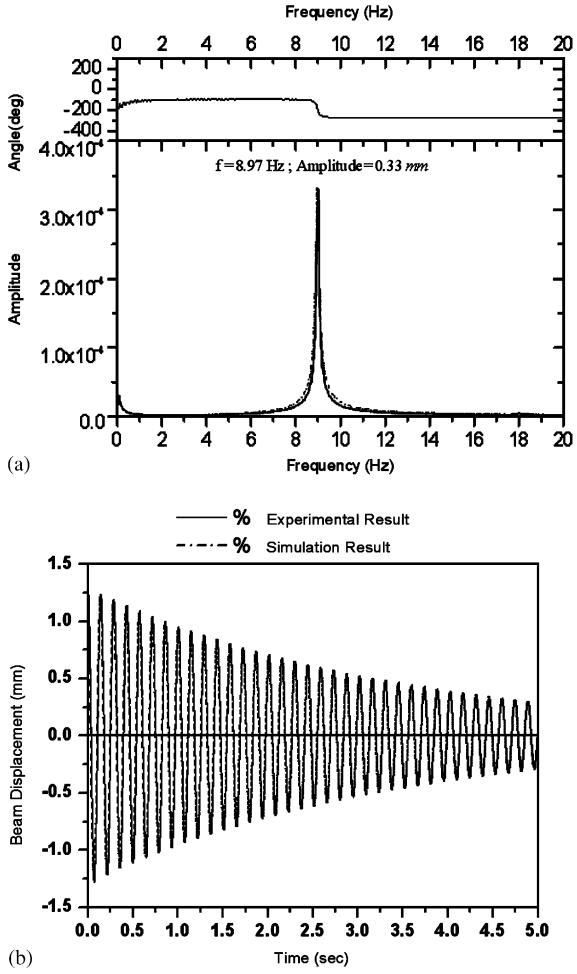

Fig. 5. (a) The amplitude and frequency of free vibration of the cantilever beam. (b) The free vibration curve of the equivalent system in the experimental operation.

corresponding resolution of 200 nm are used to observe the motion behavior of the cantilever beam. The optical-type sensor is needed to measure deflections $v(x,t)$ at $x = l$.

4.4. Numerical and experimental results

From Eqs. (2a) and (2b), we obtain the equivalent spring with the mass $M_e = 4.60 \times 10^{-3}$ kg, and the elastic constant $K_e = 14.62$ N m. By using the fast Fourier transform (FFT), the magnitudes and phase of the experiments of free vibration of the cantilever beam with a tip mass under steady-state operation are measured. Fig. 5(a) shows the measured amplitude ($\zeta\omega_n$) 0.33 mm and frequency of damped vibration ($\omega_d = \omega_n\sqrt{1-\zeta^2}$) 8.97 Hz of displacement of the cantilever beam. From Eqs. (2c) to obtain the equivalent damping constant $C_e = 2.95 \times 10^{-3}$ N s/m. We can analyze the natural frequency and cantilever beam with a tip mass parameters—the equivalent mass, stiffness, and the damping ratio. In the model analysis, the structure is assumed to be linear and the parameters to be time invariant. Fig. 5(b) shows the cantilever beam vibration curve of the equivalent model and experiment without controller, which are the vibration numerical simulation and experimental results of the cantilever beam.

The electromagnetic forces curve can use a multiple linear regression model to replace the real model. The form of multiple linear regression models and the electromagnetic forces versus air gap under different currents are shown in Fig. 6(a). Figs. 6(b)–6(d) show the electromagnetic forces versus distance, current, and distance multiplying by current regressions, the regression coefficients being $\beta_1 = 6.40 \times 10^{-3}$, $\beta_2 = 1.60 \times 10^{-2}$, and $\beta_3 = 5.46 \times 10^{-1}$, and the ANOVA analysis is listed in Table 1. The F-test statistic used to determine whether our multiple regression model is adequate is the F statistic from the preceding ANOVA table. We see that $F = 2.13 \times 10^5$ is larger than $F_{\alpha=0.01,3,1997} = 3.78$, so with right-tail area $\alpha = 0.01$, the testing procedure will be to reject $H_0 : \beta_1 = \beta_2 = \beta_3 = 0$ (this is a poor set of predictor variables), and accept the alternative hypothesis H_a: at least one $\beta \neq 0$, the three independent variables as a group are good predictors of home size. Sequentially, we use the t-test procedure to test the effect of the individual variables in the multiple regression models. For the regression coefficients, β_1, β_2, and β_3, the hypothesis $H_0 : \beta_1 = \beta_2 = \beta_3 = 0$ with a Force's three t-ratio values, $t_1 = 3.87$, $t_2 = 18.33$, and $t_3 = 19.76$, having $n - k - 1 = 1997$ degrees of freedom, there are $k = 3$ predictors, and with $n = 2001$ vectors of observations. As can be seen, all three significance levels are larger than $t_{0.005,1997}(t_{\alpha/2,n-k-1}) = 2.576$, with right-tail area $\alpha = 0.01$. Thus, we would reject the null hypothesis and accept the alternative hypothesis. Finally, in Table 1, we would get a correlation coefficient R-square value equal to 99.7%, which tells us that 99.7% of the variability in average force, from one data value to another, can be explained by distance, current, and distance multiplying by current very well.

By using the control current of the EMA in the numerical simulations and experimental operations, the magnetic attraction/repulsive forces are generated to suppress vibrations of the cantilever beam. The numerical simulations and experimental results via the PID controller are compared in Fig. 7, where the dotted lines represent the numerical simulations and the solid lines represent the experimental results. It is seen in Fig. 7(a) that the beam displacement is almost suppressed to zero within 0.5 s of proper selecting the PID control gains: $K_p = 6.5$, $K_i = 2.1$, and $K_d = 0.7$. The control current of the EMA shown in Fig. 7(b) has the peak value of 0.47 A at

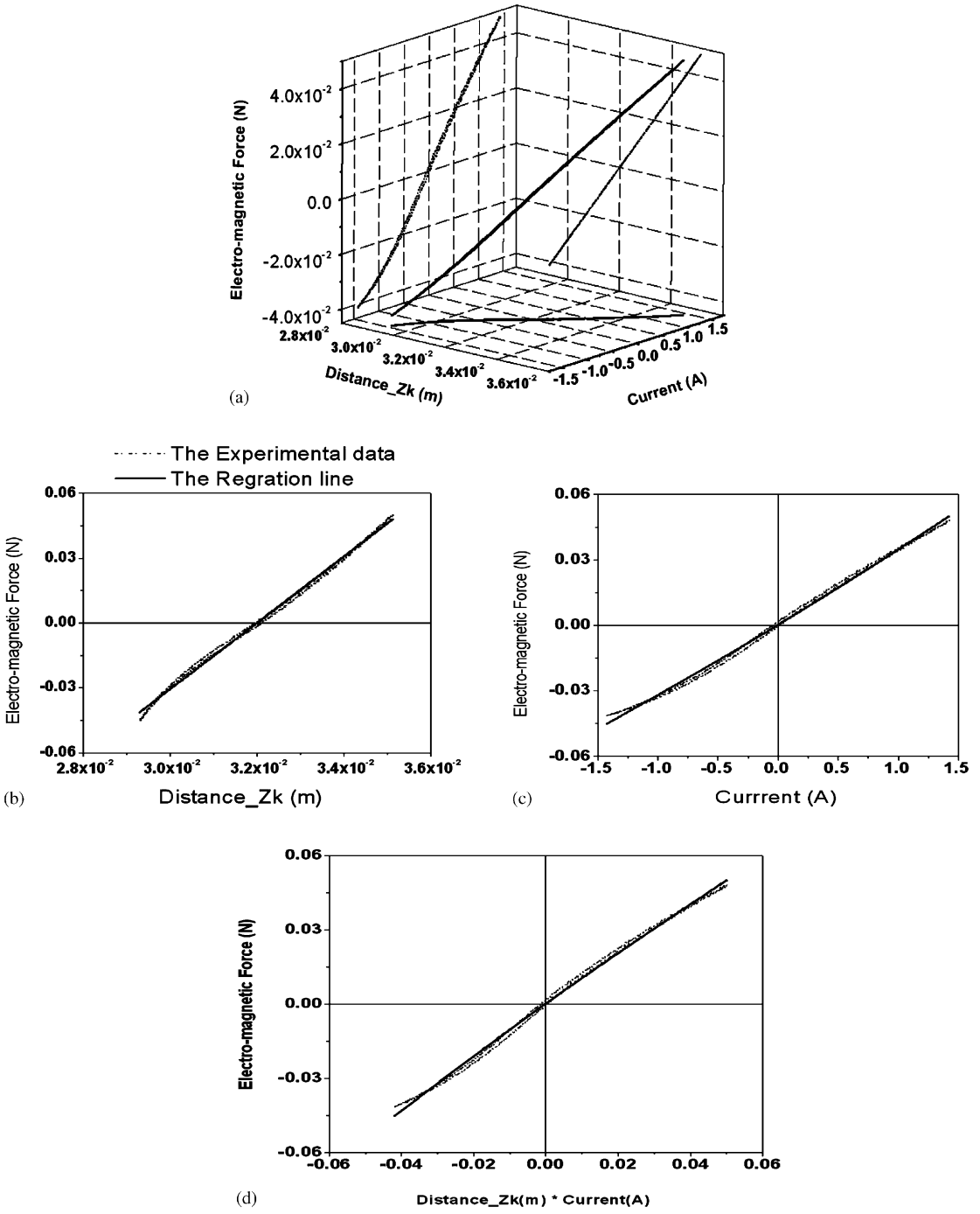

Fig. 6. (a) The multiple regressions for electromagnetic forces versus air gap under different currents. (b) The coefficient $\beta_1 = 6.40 \times 10^{-3}$ for electromagnetic forces versus distance regressions. (c) The coefficient $\beta_2 = 1.60 \times 10^{-2}$ for electromagnetic forces versus current regressions. (d) The coefficient $\beta_3 = 5.46 \times 10^{-1}$ for electromagnetic forces versus distance multiplying with current regressions.

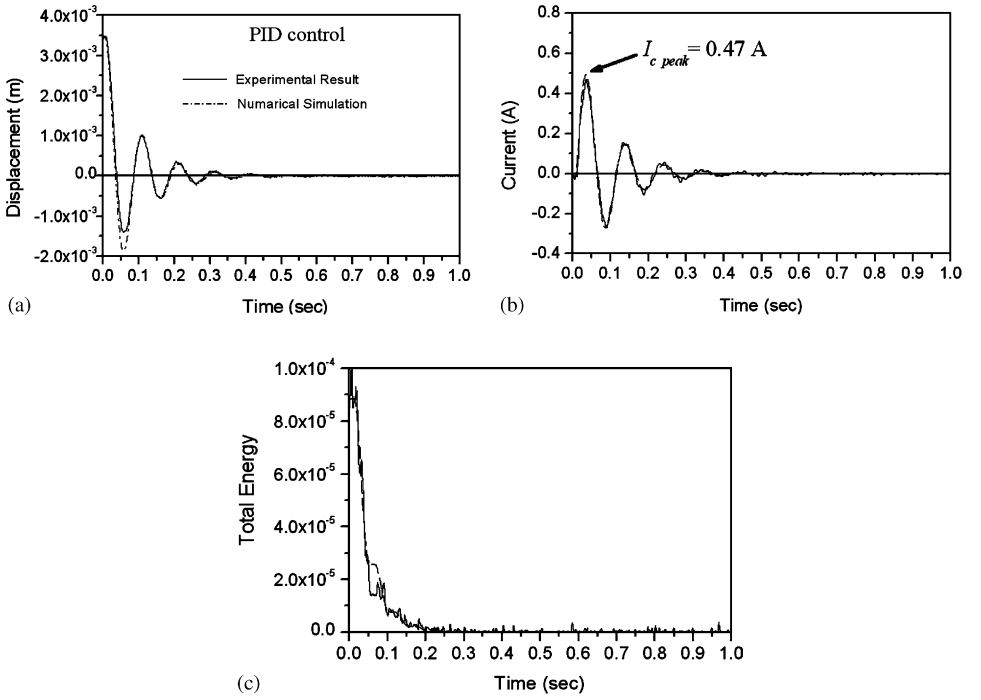

Fig. 7. The vibration control of the cantilever beam via the PID control with $K_p = 6.5$, $K_i = 2.1$, and $K_d = 0.7$. (a) The displacement of the cantilever beam. (b) The control current of the EMA. (c) The total mechanical energy.

36 ms, and will decay to zero after 0.5 s. From Eq. (2c), the total energy shown in Fig. 7(c) decays to zero after 0.3 s.

Figs. 8(a)–(c) compare the numerical simulations and experimental results of the cantilever beam via the quadratic feedback control. It is seen in Fig. 8(a) that the beam displacement is almost suppressed to zero within 0.4 s of being associated with the quadratic feedback control gain: $\alpha = 1 \times 10^{-3}$. The control current of the EMA shown in Fig. 8(b) has the peak value of 0.56 A at 26 ms, and will decay to zero after 0.4 s. The total energy shown in Fig. 8(c) decays to zero after 0.2 s.

The numerical simulations and experimental results are compared in Figs. 9(a)–(c) via the optimal feedback control. It is seen in Fig. 9(a) that the beam displacement is almost suppressed to zero within 0.25 s associated with the optimal feedback control gain: $\gamma = 0.05$. The control current of the EMA shown in Fig. 9(b) has the peak value of 0.70 A at 29 ms, and will decay to zero after 0.25 s. The total energy shown in Fig. 9(c) decays to zero after 0.15 s.

From the numerical and experimental results, we find that the controlled responses are asymptotically stable for all the three controls. From the experiences in the numerical simulations and experiment operations, a very small α value of the quadratic feedback control could not properly control the vibration, but a very large α value will cause

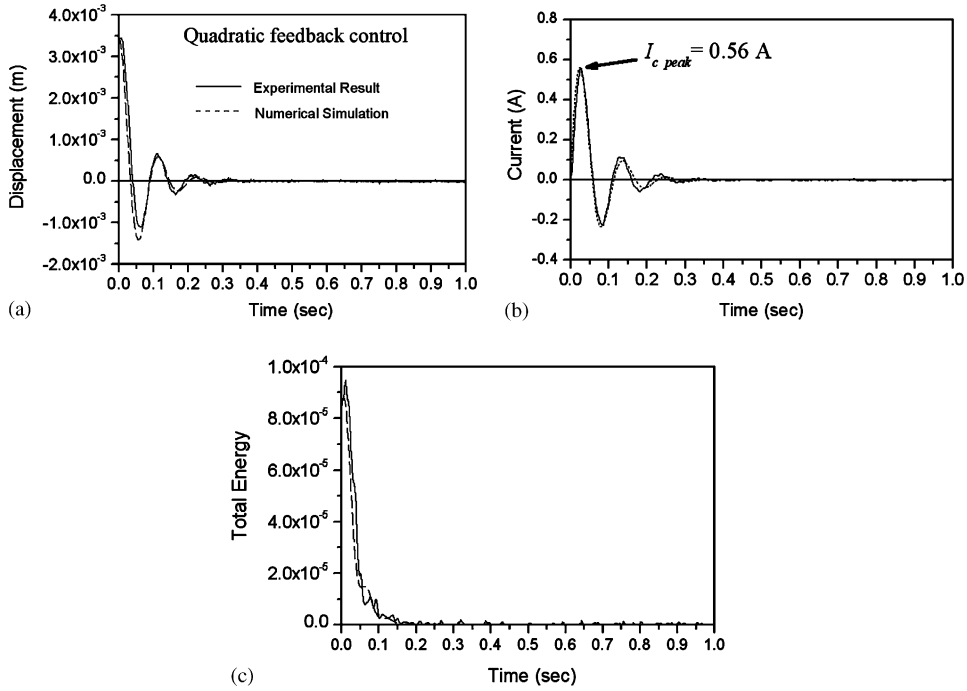

Fig. 8. The vibration control of the cantilever beam via the quadratic feedback control. (a) The disturbance displacement of the cantilever beam. (b) The control current of the EMA. (c) The total mechanical energy.

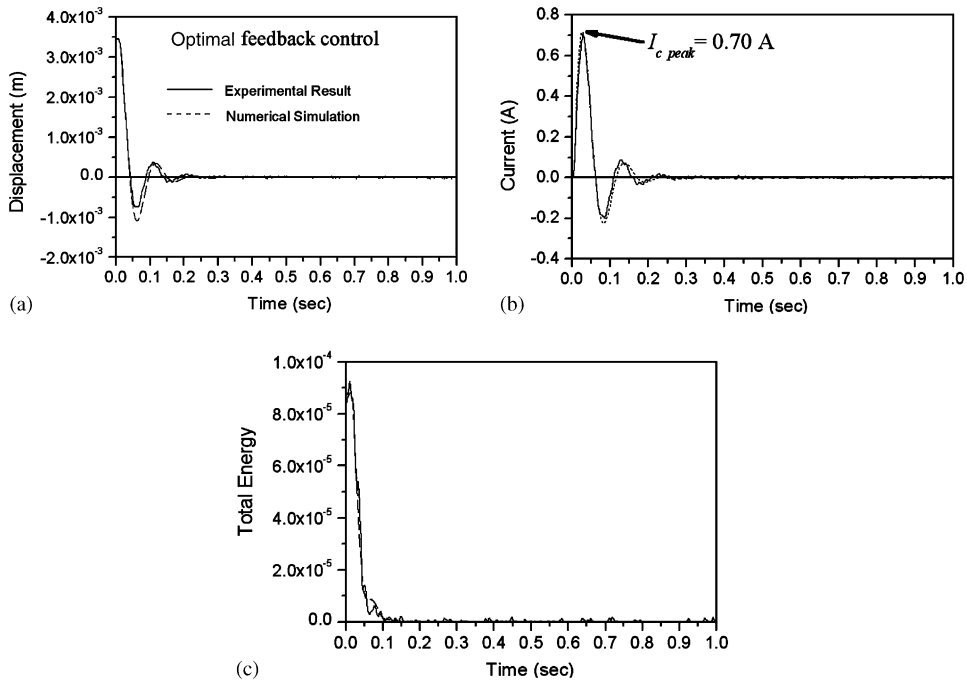

Fig. 9. The vibration control of the cantilever beam via the optimal feedback control. (a) The displacement of the cantilever beam. (b) The control current of the EMA. (c) The total mechanical energy.

the cantilever beam to hit the sensor. In summary, numerical and experimental results with the PID controller, the quadratic feedback controller and the optimal feedback controller can be effectively suppressed for the vibration control of the proposed bilinear system.

5. Conclusion

In this paper, an electromagnetic actuator for the vibration control of a cantilever beam with a tip mass is proposed. The governing equation of motion for the proposed actuator are simplified as a bilinear system, based on which three control laws including the PID control, quadratic feedback control and optimal feedback control are successfully applied to the cantilever beam system with a tip mass via the electromagnetic current. The problem is reduced to the standard form of the bilinear system. According to the numerical simulations and experimental results, it is found that the three controllers can be effectively suppressed by the vibration of a cantilever beam with a tip mass.

Acknowledgement

The authors are grateful to the National Science Council for the support under Contract no. NSC-92-2212-E-327-006.

Appendix A

In Eqs. (3)–(9), the various magnetic flux densities parameters can be seen in Ref. [4] and can be simplified as

$$\begin{aligned} F_{esx}(x,y,z) &= \int_{a_1/2}^{a_2/2}\int_{z_{e1}}^{z_{e2}} |B_{2x} - B_{4x}|\,\mathrm{d}\eta\,\mathrm{d}\xi, \\ F_{esy}(x,y,z) &= \int_{b_1/2}^{b_2/2}\int_{z_{e1}}^{z_{e2}} |B_{3y} - B_{1y}|\,\mathrm{d}\eta\,\mathrm{d}\zeta, \\ F_{esz}(x,y,z) &= \int_{a_1/2}^{a_2/2}\int_{z_{e1}}^{z_{e2}} (B_{2z} + B_{4z})\,\mathrm{d}\eta\,\mathrm{d}\xi, \\ &\quad + \int_{b_1/2}^{b_2/2}\int_{z_{e1}}^{z_{e2}} (B_{1z} + B_{3z})\,\mathrm{d}\eta\,\mathrm{d}\zeta, \end{aligned} \tag{A.1}$$

where ξ, ζ, η are variables of integration in x, y, and z directions, respectively. If we consider the coil with a number of turns N, B_{1z} represent the magnetic flux densities at the coordinate z due to bundled conductors AB under a current I, while B_{1y} represent

the magnetic flux densities at the coordinate y due to bundled conductors AB under a current I.

$$
\begin{aligned}
B_{1P} &= \varepsilon_1 \frac{I}{4\pi R_1}(\cos\,\theta_{11} - \cos\,\theta_{12}),\\
B_{1z} &= B_{1P}\ \cos\,\phi_1 = \varepsilon_1 \frac{I}{4\pi R_1}(\cos\,\theta_{11} - \cos\,\theta_{12})\ \cos\,\phi_1,\\
B_{1y} &= B_{1P}\ \sin\,\phi_1 = \varepsilon_1 \frac{I}{4\pi R_1}(\cos\,\theta_{11} - \cos\,\theta_{12})\ \sin\,\phi_1,
\end{aligned}
\tag{A.2}
$$

where

$$
R_1 = [(\zeta + y)^2 + (z - \eta)^2]^{1/2}, \quad \varepsilon_1 = \begin{cases} 1, & y \geqslant -\zeta, \\ -1, & y < -\zeta, \end{cases}
$$

$$
\theta_{11} = \begin{cases} \tan^{-1}\left[\frac{R_1}{\frac{a_1}{2}+(\zeta-\frac{b_1}{2})+x}\right] & \text{for } x > -\left[\frac{a_1}{2}+(\zeta-\frac{b_1}{2})\right], \\ \pi - \tan^{-1}\left[\frac{-R_1}{\frac{a_1}{2}+(\zeta-\frac{b_1}{2})+x}\right] & \text{for } x < -\left[\frac{a_1}{2}+(\zeta-\frac{b_1}{2})\right], \\ \frac{\pi}{2} & \text{for } x = -\left[\frac{a_1}{2}+(\zeta-\frac{b_1}{2})\right], \end{cases}
$$

$$
\theta_{12} = \begin{cases} \pi - \tan^{-1}\left[\frac{R_1}{\frac{a_1}{2}+(\zeta-\frac{b_1}{2})-x}\right] & \text{for } x < \left[\frac{a_1}{2}+(\zeta-\frac{b_1}{2})\right], \\ \tan^{-1}\left[\frac{-R_1}{\frac{a_1}{2}+(\zeta-\frac{b_1}{2})-x}\right] & \text{for } x > \left[\frac{a_1}{2}+(\zeta-\frac{b_1}{2})\right], \\ \frac{\pi}{2} & \text{for } x = \left[\frac{a_1}{2}+(\zeta-\frac{b_1}{2})\right], \end{cases}
$$

$$
\phi_1 = \sin^{-1}\left[(z - \eta)/R_1\right].
$$

The magnetic flux densities due to the current BC,CD and DA can be obtained in the same way.

$$
\begin{aligned}
F_{ecx}(x, y, z) &= \int_{z_3}^{z_2} |B_{2x} - B_{4x}|_{\xi = a_1/2}\, \mathrm{d}\eta,\\
F_{ecy}(x, y, z) &= \int_{z_3}^{z_2} |B_{3y} - B_{1y}|_{\zeta = b_1/2}\, \mathrm{d}\eta,\\
F_{ecz}(x, y, z) &= \int_{z_3}^{z_2} (B_{1z} + B_{2z} + B_{3z} + B_{4z})_{\xi = a_1/2, \zeta = b_1/2}\, \mathrm{d}\eta.
\end{aligned}
\tag{A.3}
$$

In Eq. (5):

$$
\begin{aligned}
G_{\mathrm{P}} &= \sqrt{G_{px}^2 + G_{py}^2 + G_{pz}^2},\\
G_{c\mathrm{P}} &= \sqrt{G_{cpx}^2 + G_{cpy}^2 + G_{cpz}^2},\\
G_{px} &= \int_{-a_1/2}^{a_1/2}\int_{-b_1/2}^{b_1/2}\int_{z_2}^{0} |B_{2x} - B_{4x}|_{\xi=a_1/2,z=z_2}\,\mathrm{d}\eta\,\mathrm{d}y\,\mathrm{d}x,\\
G_{py} &= \int_{-a_1/2}^{a_1/2}\int_{-b_1/2}^{b_1/2}\int_{z_2}^{0} \left|B_{3y} - B_{1y}\right|_{\zeta=b_1/2,z=z_2}\,\mathrm{d}\eta\,\mathrm{d}y\,\mathrm{d}x,\\
G_{pz} &= \int_{-a_1/2}^{a_1/2}\int_{-b_1/2}^{b_1/2}\int_{z_2}^{0} (B_{1z} + B_{2z} + B_{3z} + B_{4z})_{\xi=a_1/2,\zeta=b_1/2,z=z_2}\,\mathrm{d}\eta\,\mathrm{d}y\,\mathrm{d}x,\\
G_{cpx} &= \int_{-a_1/2}^{a_1/2}\int_{-b_1/2}^{b_1/2}\int_{z_3}^{z_2} |B_{2x} - B_{4x}|_{\xi=a_1/2,z=z_2}\,\mathrm{d}\eta\,\mathrm{d}y\,\mathrm{d}x,\\
G_{cpy} &= \int_{-a_1/2}^{a_1/2}\int_{-b_1/2}^{b_1/2}\int_{z_3}^{z_2} \left|B_{3y} - B_{1y}\right|_{\zeta=b_1/2,z=z_2}\,\mathrm{d}\eta\,\mathrm{d}y\,\mathrm{d}x,\\
G_{cpz} &= \int_{-a_1/2}^{a_1/2}\int_{-b_1/2}^{b_1/2}\int_{z_3}^{z_2} (B_{1z} + B_{2z} + B_{3z} + B_{4z})_{\xi=a_1/2,\zeta=b_1/2,z=z_2}\,\mathrm{d}\eta\,\mathrm{d}y\,\mathrm{d}x.
\end{aligned}
\tag{A.4}
$$

In Eq. (6):

$$
\begin{aligned}
F_{px}(x,y,z) &= \int_{z_2}^{0} |B_{2x} - B_{4x}|_{\xi=a_1/2}\,\mathrm{d}\eta,\\
F_{py}(x,y,z) &= \int_{z_2}^{0} \left|B_{3y} - B_{1y}\right|_{\zeta=b_1/2}\,\mathrm{d}\eta,\\
F_{pz}(x,y,z) &= \int_{z_2}^{0} (B_{1z} + B_{2z} + B_{3z} + B_{4z})_{\xi=a_1/2,\zeta=b_1/2}\,\mathrm{d}\eta.
\end{aligned}
\tag{A.5}
$$

In Eq. (7):

$$
\begin{aligned}
F_{mx}(x,y,z) &= \int_{z_2}^{0} |B_{2x} - B_{4x}|_{\xi=a_1/2}\,\mathrm{d}\eta,\\
F_{my}(x,y,z) &= \int_{z_2}^{0} \left|B_{3y} - B_{1y}\right|_{\zeta=b_1/2}\,\mathrm{d}\eta,\\
F_{mz}(x,y,z) &= \int_{z_2}^{0} (B_{1z} + B_{2z} + B_{3z} + B_{4z})_{\xi=a_1/2,\zeta=b_1/2}\,\mathrm{d}\eta.
\end{aligned}
\tag{A.6}
$$

Appendix B

In Eq. (11c), the polynomial regression functions are used and the coefficients are obtained as

$$\begin{aligned}\alpha_2(z_k) &= \frac{1}{2\mu_0}\int_{-a_1/2}^{a_1/2}\int_{-b_1/2}^{b_1/2}[K_1^2(F_{esz}^2 - F_{esx}^2 - F_{esy}^2) + 2K_1K_2(F_{esz}F_{ecz} - F_{esx}F_{ecx} - F_{esy}F_{ecy}) \\ &\quad + K_2^2(F_{ecz}^2 - F_{ecx}^2 - F_{ecy}^2)]\,\mathrm{d}x\,\mathrm{d}y \\ &= \beta_{20} + \beta_{21}z_k + \beta_{22}z_k^2 + \beta_{23}z_k^3,\end{aligned}$$

$$\begin{aligned}\alpha(z_k) &= \frac{1}{\mu_0}\int_{-a_1/2}^{a_1/2}\int_{-b_1/2}^{b_1/2}\{K_1[F_{esz}(B_{pz} - B_{mz}) - F_{esx}(B_{px} - B_{mx}) - F_{esy}(B_{py} - B_{my})] \\ &\quad + K_2[F_{ecz}(B_{pz} - B_{mz}) - F_{ecx}(B_{px} - B_{mx}) - F_{ecy}(B_{py} - B_{my})]\}\,\mathrm{d}x\,\mathrm{d}y \\ &= \beta_{10} + \beta_{11}z_k + \beta_{12}z_k^2 + \beta_{13}z_k^3,\end{aligned}$$

$$\begin{aligned}F_s(z_k) &= \frac{1}{2\mu_0}\int_{-a_1/2}^{a_1/2}\int_{-b_1/2}^{b_1/2}[(B_{pz} - B_{mz})^2 - (B_{px} - B_{mx})^2 - (B_{py} - B_{my})^2]\,\mathrm{d}x\,\mathrm{d}y \\ &= \beta_{00} + \beta_{10}z_k + \beta_{02}z_k^2 + \beta_{03}z_k^3,\end{aligned} \tag{B.1}$$

where

$$K_1 = \frac{N}{(\frac{a_2}{2} - \frac{a_1}{2})H} = \frac{N}{(\frac{b_2}{2} - \frac{b_1}{2})H} \quad \text{and} \quad K_2 = \mu\frac{N}{z_2} = \mu_0\mu_r\frac{N}{z_2}.$$

Appendix C

The forces generated by the electromagnetic actuator for various input currents and air gaps are depicted in Fig. 6. From the experimental results, the control force of the EMA is reduced to

$$F_c(z_k, I) \approx \beta_1 z_k + \beta_2 I + \beta_3 z_k I. \tag{C.1}$$

The form of multiple regression method [14] offers the behavior of a particular dependent variable $F_c(z_k, I)$ based on the three predictor variables $(z_k, I, z_k I)$. It can use a computerized statistical package such as EXCECL, MINITAB, SPSS, STATISTICS, or SAS to estimate the coefficients of the force. To determine adequacy of the regression model, we can test the entire set of predictor variables using an F test 3 (k) and 1997 ($n - k - 1$) degrees of freedom. The contribution of an individual predictor variable (say, $z_k, I, z_k I$) can be tested using a t statistic with 1997 ($n - k - 1$) degrees of freedom. The ANOVA analysis table is listed in Table 1.

The solution for the preceding illustration is shown in Table 1. Using the results, the F value is larger than $F_{\alpha=0.01,3,1997} = 3.78$ (reject $\mathrm{H}_0 : \beta_1 = \beta_2 = \beta_3 = 0$), which owns the highest correlation (R square = 99.7%). The three independent variables as a group are good predictors of home size. According to Table 1, the three t-ratio values are larger than $t_{0.005,1997}(t_{\alpha/2,n-k-1}) = 2.576$. A large value of t-ratio indicates that Z_k, I, and $Z_k I$ contribute significantly to the prediction of $F_c(z_k, I)$.

References

[1] B.E. Schafer, H. Holzach, Experimental researches on flexible beam modal control, *Journal of Guidance, Control, and Dynamics* 8 (5) (1985) 597–604.
[2] M.S. Ju, Y.Y. Chung, Y.G. Tsuei, Development of electromagnetic actuators for structure control, *Journal of Control Systems and Technology* 1 (3) (1993) 235–246.
[3] K. Nagaya, N. Arai, Analysis of a permanent magnet levitation actuator with electromagnetic control, *Journal of Dynamic Systems, Measurement, and Control* 113 (1991) 472–478.
[4] K. Nagaya, M. Ishikawa, A noncontact permanent magnet levitation table with electromagnetic control and its vibration isolation method using direct disturbance cancellation combining optimal regulators, *IEEE Transactions on Magnetics* 31 (1) (1995) 885–896.
[5] K. Nagaya, M. Sugiura, A method for obtaining a linear spring for a permanent magnet levitation system using electromagnetic control, *IEEE Transactions on Magnetics* 31 (3) (1995) 2332–2338.
[6] R.R. Mohler, *Nonlinear Systems: Vol. II, Applications to Bilinear Control*, Prentice-Hall, Englewood Cliffs, NJ, 1991.
[7] P.O. Gutman, Stabilizing controllers for bilinear systems, *IEEE Transactions on Automatic Control* 26 (4) (1981) 917–922.
[8] W.A. Cebuhar, V. Costanza, Approximation procedures for the optimal control of bilinear and nonlinear systems, *Journal of Optimization Theory and Applications* 43 (4) (1984) 615–627.
[9] D. Benallou, D.A. Mellichamp, D.E. Seborg, Optimal stabilizing controllers for bilinear systems, *International Journal of Control* 48 (4) (1988) 1487–1501.
[10] M.S. Chen, Exponential stabilization of a constrained bilinear system, *Automatica* 34 (8) (1998) 989–992.
[11] J.A. Stratton, *Electromagnetic Theory*, McGraw-Hill, New York, 1941.
[12] W.T. Thomson, *Theory of Vibration with Applications*, Prentice-Hall, Englewood Cliffs, NJ, 1981.
[13] S.R. Singiresu, *Mechanical Vibrations*, Addison-Wesley, New York, 1990.
[14] R.R. Wilcox, *Statistics for the Social Sciences*, Academic Press, California, 1996.
[15] F.L. Lewis, V.L. Syrmos, *Optimal Control*, Wiley, New York, 1995.
[16] W.A. Cebuhar, V. Costanza, Approximation procedures for the optimal control of bilinear and nonlinear systems, *Journal of Optimization Theory and Applications* 43 (4) (1984) 615–627.
[17] A.E. Bryson Jr., Y.C. Ho, *Applied Optimal Control*, Wiley, New York, 1975.